Composites Part B 256 (2023) 110649

Contents lists available at ScienceDirect

Composites Part B

journal homepage: www.elsevier.com/locate/compositesb

Flower-like strontium molybdate anchored on 3D N-rich reduced graphene oxide aerogel composite: An efficient catalyst for the detection of lethal pollutant nitrobenzene in water samples

Raj Karthik [a,1], Prajakta R. Chavan [a,1], Ramaraj Sukanya [a,1,*], Ganesh Dhakal [a], Jae-Jin Shim [a,**], Carmel B. Breslin [b,***]

[a] School of Chemical Engineering, Yeungnam University, Gyeongsan, Gyeongbuk, 38541, Republic of Korea
[b] Department of Chemistry, Maynooth University, Maynooth, Co. Kildare, Ireland

ARTICLE INFO

Handling Editor: Prof. Joong Lee

Keywords:
Flower-like $SrMoO_4$
3D N-rich rGO
Lethal pollutant
Nitrobenzene
Water samples

ABSTRACT

Nitrobenzene (NB) is a carcinogenic water pollutant that can have dangerous effects on humans, animals, and the environment even in trace amounts. It can persist in contaminated sites and leach into the adjacent aquatic environment. Therefore, the detection of trace amounts of NB is of great interest. To address this challenge, we have fabricated strontium molybdate microflowers ($SrMoO_4$, SMO MFs) grown on nitrogen-rich, porous three-dimensional (3D) reduced graphene oxide aerogels (SMO/N-rGO) for sensitive detection of NB in water samples. The 3D N-rGO and SMO/N-rGO composites were prepared by simple hydrothermal and precipitation methods. The fabricated SMO/N-rGO composites exhibited a porous and 3D structure with a strong synergistic effect between the SMO MFs and the N-rich porous rGO sheets with open voids that facilitate the diffusion of NB. The electrochemical detection of NB at the SMO/N-rGO modified electrode was significantly enhanced. Using amperometry (*i-t*), the modified SMO/N-rGO sensor was shown to have two linear response ranges in the sensing of NB, with the lower linear concentration range from 7.1 nM to 1.0 mM and the higher linear concentration range varying from 1.1 mM to 2.5 mM. In addition, the limit of detection (LOD) was calculated to be 2.1 nM using the amperometric (*i-t*) technique. Common nitro derivatives, biomolecules, and cations often found in water systems had no influence on the detection of NB. At the same time, a good recovery of 96.1–99.6% was obtained for real-time monitoring analysis in tap and lake water samples. In this work, new electrochemical sensors for monitoring various pollutants are developed based on anchoring conductive metal oxide electrocatalysts on porous 3D carbon aerogels.

1. Introduction

The pollution of aquatic environments, including drinking water, through the discharge of industrial wastes, is becoming more of a serious issue with further population growth. One of the most toxic chemicals found as water contaminants is aromatic compounds with nitro groups, and these are considered highly toxic, carcinogenic, and mutagenic [1,2]. Among them, nitrobenzene (NB), which is still widely used in the production of dyes, pesticides, and explosives [3,4], is a major concern. It has been found in groundwater in China, and given its stability, it can easily migrate to rivers and other aquatic sources to cause significant pollution [5]. Of particular concern are abandoned NB contaminated sites that can continue to pollute the surrounding environment, and it is estimated that some 2.8 million contaminated sites may exist in Europe [6]. NB can cause serious health problems, such as shortness of breath, vomiting, and nausea [7,8]. It can enter the human body on contact with skin or through the respiratory tract, and if not treated medically it can give rise to coma and possible death [9,10]. It is also very toxic to all aquatic life. Due to its hazardous nature, it has been classified as a B2 carcinogen by the US Environmental Protection Agency (USEPA).

* Corresponding author.
** Corresponding author.
*** Corresponding author.
E-mail addresses: sukanyaram33@gmail.com (R. Sukanya), jjshim@yu.ac.kr (J.-J. Shim), Carmel.Breslin@mu.ie (C.B. Breslin).
[1] The authors R. Karthik, Prajakta R. Chavan, and R. Sukanya contributed equally to this work.

https://doi.org/10.1016/j.compositesb.2023.110649
Received 9 November 2022; Received in revised form 4 February 2023; Accepted 24 February 2023
Available online 28 February 2023
1359-8368/

Therefore, the detection of NB at trace levels in the aquatic environment is essential. Various chromatographic [11] and spectrophotometric [12] methods have been developed and used for detecting and determining NB in wastewater. However, most of these techniques require sample preparation, are time-consuming, with complex and high-cost instrumentation, and suffer from insufficient sensitivity, which limits their usefulness for practical applications [13–18]. On the other hand, the electrochemical analysis of NB has the advantage of rapid on-site analysis combined with simple operation and low cost, which makes it more suitable for routine detection and analysis of NB in the aquatic environment. Besides, the electrochemical sensor and electrodes based on it have many advantages, such as the ability to detect the target molecules at very low levels, a broader linear response range, a simple surface renewal procedure, high sensitivity, and acceptable reproducibility, repeatability, and selectivity compared to other traditional techniques. Indeed, the merits of electrochemical techniques in sensing applications are clearly documented in the literature for a variety of molecules [19–25].

Different nano/microstructural materials have been developed and used for the sensitive electrochemical detection of NB, including indium tin oxide [7] and graphene oxide electrodes [8] which were further modified with cyclodextrins to give selectivity. In other studies, niobium-doped boron-carbon-nitrogen nanotubes [26], iron oxides [27], and nitrogen-doped porous carbon [28] have been employed successfully. In many of these cases, the research has centered on the electrocatalytic activity of the fabricated sensors [29,30], with less focus on the analytical characteristics, including the analysis of real water samples. While cyclodextrins have supramolecular properties and can form inclusion complexes with benzene-like molecules when simply combined with an electrocatalyst, they can be easily lost from the sensor surface [8,10]. Furthermore, the electrochemical reduction of NB is complex [28] with multiple electron/proton transfer steps. Therefore, the development of low-cost and sustainable electrocatalysts that can be used to give both the selective and sensitive detection of NB remains a challenge. In this paper, we aim to show that metal molybdates combined with nitrogen-rich reduced graphene oxide (N-rGO) aerogels can be employed as a cost-effective and high-performing sensor for the detection of trace amounts of NB.

The metal molybdates ($MMoO_4$; M = Ba, Ca, Sr, and Mg) show admirable electrochemical applications due to their excellent strength, cost-effectiveness, environmental friendliness, non-toxicity, abundance, ease of synthesis, and multiple oxidation states. They also exhibit good biocompatibility and high decomposition temperature, with high chemical/physical properties and mechanical stability [31]. Among them, strontium is an interesting metal from an electrochemical viewpoint, and strontium molybdate (scheelite-type $SrMoO_4$; SMO) has been employed in the construction of electrochemical sensors for the sensing of acebutolol [32] and chlorpromazine [33]. SMO has attractive physical/chemical properties, low-cost, simple synthesis steps with high yields, excellent thermal stability, and earth abundance [32]. Also, the electrochemical performance of SMO is derived from the charge distribution between the Sr^{2+} and $[MoO_4]^{2-}$ units [31]. Based on the literature results and the electrochemical properties of SMO, the authors were inspired to construct a flower-like SMO by a simple synthesis method and its electrochemical sensing application for the detection of NB. The electrochemical behavior and stability of the metal molybdate can be further improved by combining it with carbon. For example, *Karthik* et al. described the preparation of ytterbium molybdate anchored onto carbon nanofibers (YbM/f-CNFs) for the electrochemical and photochemical detection of pollutants [34].

In this paper, reduced graphene oxide (rGO), a well-known material for electrochemical sensing applications with very good electrical conductivity and chemical stability, was selected as the carbon support. To minimize the aggregation of the rGO sheets, which can limit their electrochemical applications [35–37], a 3D porous rGO aerogel was employed. These 3D porous aerogels with adjustable pores and large surface areas are emerging as an electrochemical sensing platform [36,38] with internally connected hollow meshes, enhanced conductivity, improved stability, and the presence of large voids for ion diffusion [38,39]. Furthermore, the rGO aerogels can be doped with heteroatoms, such as nitrogen and sulfur [40–42], to reduce the charge transfer resistance and improve the electrochemical sensing performance [38]. The N dopants can bond with C to alter the charge distribution and spin density, which, in turn, enhances the electrocatalytic activity [43,44]. In the case of rGO, the N atom in the graphene lattice exerts a pronounced synergistic effect, leading to more defects and a tunable electronic structure [45,46]. Indeed, N-doped rGO aerogels, have been developed and used as sensors in the detection of bisphenol and hydrogen peroxide [38].

In this work, we combined the porous, large surface area and tunable electronic properties of N-rGO aerogels with flower-like $SrMoO_4$ (SMO) structures by anchoring them on the surface of N-rich rGO aerogel (SMO/N-rGO). We first synthesized an N-rich rGO aerogel by a hydrothermal process, and the flower-like SMO was grown on the N-rGO surface by a simple precipitation method. The synergistic interaction between the SMO and the mutually cross-linked N-rich porous rGO aerogel was evaluated and confirmed by different analytical and spectroscopic techniques. Finally, the SMO/N-rGO modified electrode was successfully used for the electrochemical determination of NB. Voltammetry and amperometry (*i-t*) techniques were used to investigate the electrochemical performance of the NB sensor. The SMO/N-rGO-based sensor showed excellent electrochemical properties with a low detection limit and high sensitivity for the reduction of NB and was successfully used for the practical determination of NB in various water samples.

2. Experimental section

2.1. Synthesis of SMO MFs, N-rGO aerogel, and SMO/N-rGO composite

Detailed information on chemicals and reagents, material characterization, and electrode preparation can be found in the Supplementary file (sections *S2.1 - S2.3*). Graphene oxide (GO) was prepared by the modified Hummer's method as described in a previous report (Scheme 1 (a)), while N-rGO was prepared with slight modifications [47]. The detailed preparation of the N-rGO aerogel is clearly shown in the supplementary file (sections *S2.4*).

For the preparation of SMO/N-rGO, 10 mg N-rGO was dispersed in 35 mL of deionized water in a sonicator bath for 10 min. Then, with constant stirring, 12.5 mM $SrCl_2.6H_2O$ was added to the N-rGO dispersion. The above mixture was stirred for 15 min. A 25 mM $Na_2MoO_4.2H_2O$ was prepared separately in 35 mL of deionized water and stirred for 10 min to obtain a homogeneous solution. Then the $Na_2MoO_4.2H_2O$ solution was added dropwise to the N-rGO/$SrCl_2$ containing mixture with continuous stirring. The mixture tends to show some turbidity when $Na_2MoO_4.2H_2O$ is added. Then 7 mL of EG was added to this mixture and stirred for 1 h. The obtained precipitate was washed with deionized water to remove the unreacted material and filtered. The product (Scheme 1(b)) was dried overnight in a vacuum oven at 60 °C. For comparison, the weight ratio of N-rGO (i.e., 5, 10, and 15 mg) was optimized with SMO MFs, SMO MFs (Scheme 1(c)) was also prepared without N-rGO, and rGO was prepared without hydrazine. The overall synthesis procedure of SMO MFs, N-rGO aerogel and SMO/N-rGO composite is shown and summarized in Scheme 1.

3. Results and discussion

3.1. Morphological studies of flower-like SMO, rGO, 3D N-rGO aerogel, and SMO/N-rGO composite

The SMO micro flowers (MFs) were synthesized by the reaction between Sr^{2+} and $[MoO_4]^{2-}$ ions in the presence of the structural directing

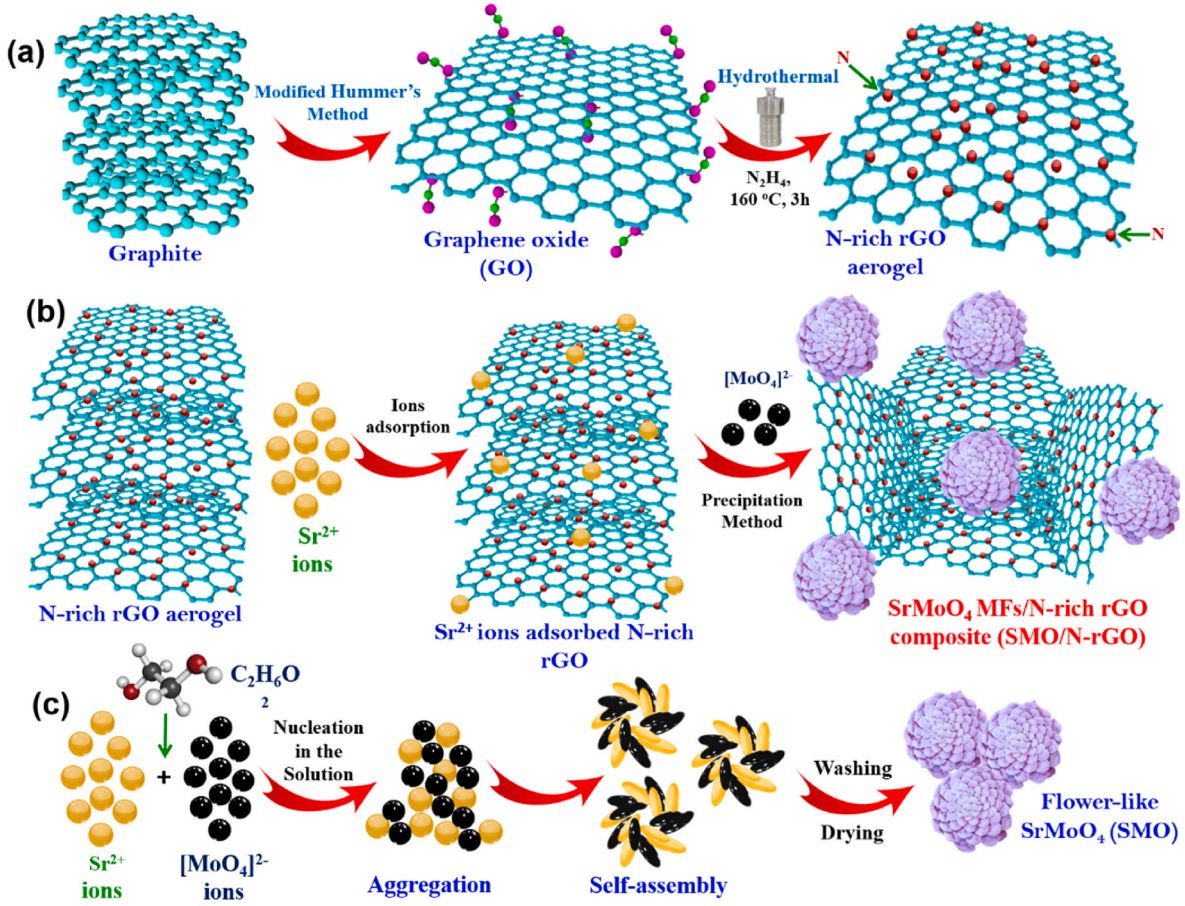

Scheme 1. Schematic illustration of the synthesis procedure of (a) N-rGO aerogel, (b) SMO/N-rGO, and (c) SMO MFs.

agent EG by a simple co-precipitation method at room temperature to give flower-like SMO structures. The morphology of these SMO microstructures was investigated by FE-SEM analysis, and the corresponding images are shown in Fig. 1. As can be seen in Fig. 1(a and b), the images from FE-SEM show that the SMO has the shape of flower-like structures with diameters of about 3–5 μm. These MFs are composed of large individual seeds with porous surfaces that combine to form a micro-sized SMO. The size of the individual seed particles and the thickness of the individual seeds are in the micrometer range. Fig. 1(b, top inset) shows the bottom surface of the fabricated SMO, which is porous and has a strong base for SMO growth. The weight percentages of the SMO MFs are listed in Table S1, with the weight percentages of Mo (39.39), O (32.54), and Sr (28.07). No other by-products or impurities were observed, demonstrating the good purity of the prepared SMO MFs. The FE-SEM images of rGO and N-rGO are shown in Fig. 1(c–f). The rGO is twisted with porous multilayer graphene sheets and consists of interconnected hierarchical ribbed graphene layers. Accordingly, the rGO sheets are wrinkled and flexible, which contrasts with the typical graphite structure. As evident in Fig. 1(e and f), the FE-SEM images of N-rich rGO exhibit a three-dimensional (3D) porous structure with wrinkled graphene layers, folds, and crimped edges [47] to give a high surface area. Compared to rGO, under the same hydrothermal conditions, it is evident that the N-rGO aerogel exhibits more wrinkled and curved layers and forms a pore-rich 3D structure. This is consistent with the incorporation of the N atoms into the graphene layer, which breaks the two-dimensional (2D) plane of graphene, resulting in curvature, with the interactions between these curled layers forming a more porous structure [41]. The FE-SEM images of the SMO/N-rGO composite at different magnifications show the successful attachment of the SMO MFs on the surface of the N-rGO aerogel, as shown in Fig. 1(g and h). The EDX analysis presented in Fig. 1(i) confirms the presence of C, N, O, Sr and Mo, while the elemental mapping analysis presented in Fig. 1(i) and j-(o) shows good distribution of all the elements, C, N, O, Sr, and Mo. The corresponding weight and atomic percentages of all the elements are tabulated in Fig. 1(p), with the atomic % of Mo (0.56) and Sr (0.37) in reasonably good agreement with a ratio of 1:1 for $SrMoO_4$. More information on the surface features and lattice distortions of the SMO/N-rGO composite was obtained using FE-TEM, and the corresponding images for N-rGO and SMO/N-rGO are shown in Fig. 2. These images clearly indicate the formation of an N-rich rGO aerogel and N-rGO decorated with SMO MFs. The FE-TEM image of the N-rGO aerogel (Fig. 2(a)) shows the presence of a transparent multi-graphene layer with a much more corrugated and wrinkled structure. This wrinkled structure increases the surface area, and reduces aggregation (π- π stacking interaction), thus facilitating the formation of a porous 3D surface.

The images in Fig. 2 are consistent with the previously published work on N-rich graphene-based aerogel composites [47]. Fig. 2(b) shows the presence of an amorphous structure (lattice image of N-rGO), which is probably due to the presence of a larger number of defects and nitrogen groups in the graphene plane. The high N and O contents indicate the successful formation of an N-rich rGO aerogel by removing a minimal amount of oxygen. The presence of the SMO MFs and the successful anchoring of the SMO MFs on the N-rGO aerogel are seen in Fig. 2(c and d). It is also clear that the morphology of the SMO MFs is not affected by the introduction of N-rGO, and there is no evidence of aggregation of the SMO MFs on the surface of the N-rGO aerogel. The lattice distortion of the SMO MFs and the N-rGO can be clearly seen in the high-resolution lattice fringe image in Fig. 2(e). It shows a well-defined lattice fringe with a d-spacing of 0.36 and 0.32 nm, corresponding to the (002) and

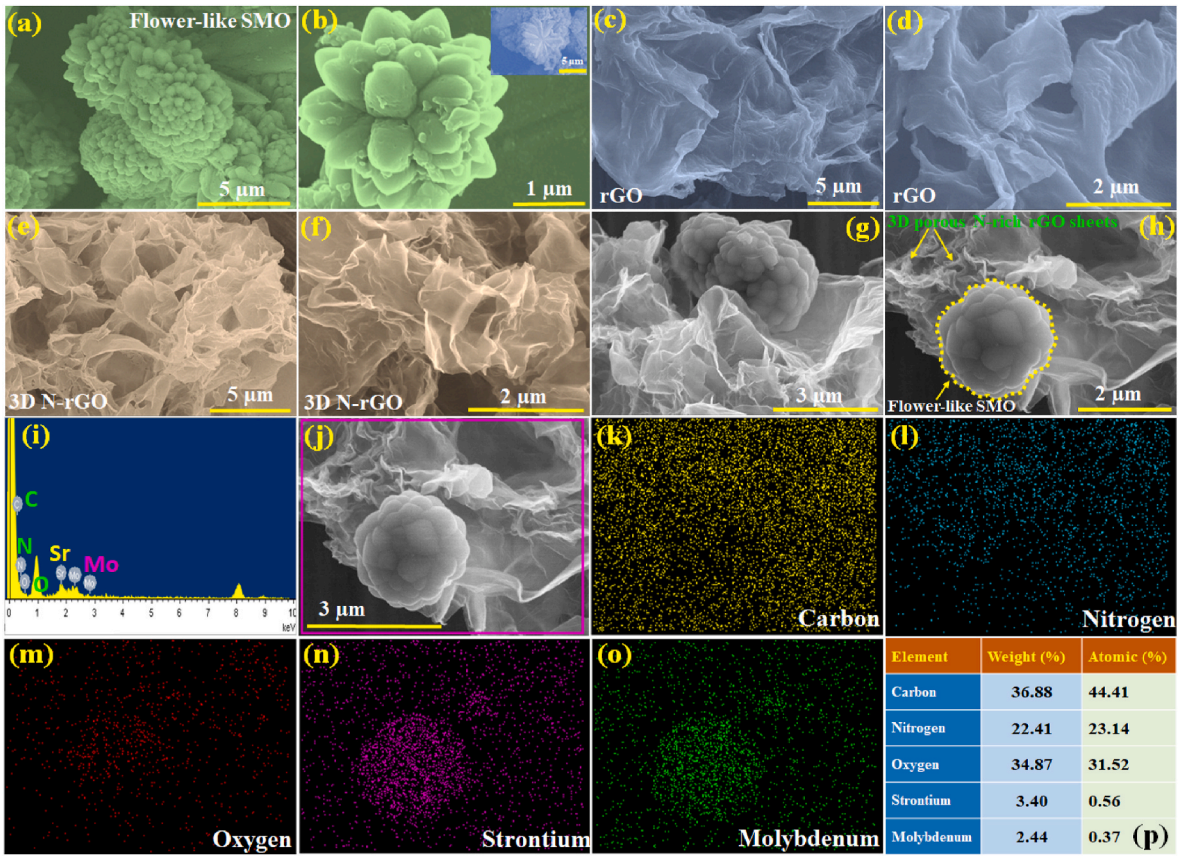

Element	Weight (%)	Atomic (%)
Carbon	36.88	44.41
Nitrogen	22.41	23.14
Oxygen	34.87	31.52
Strontium	3.40	0.56
Molybdenum	2.44	0.37

Fig. 1. Low and high magnification FE-SEM images of (a, b) flower-like SMO, (c, d) rGO, (e, f) 3D N-rich rGO aerogel, (g, h) SMO/N-rGO composite. (i) EDX, (j–o) element mapping analysis, and (p) element atomic and weight percent of SMO/N-rGO composite. (b) The inset shows the base of the SMO MFs.

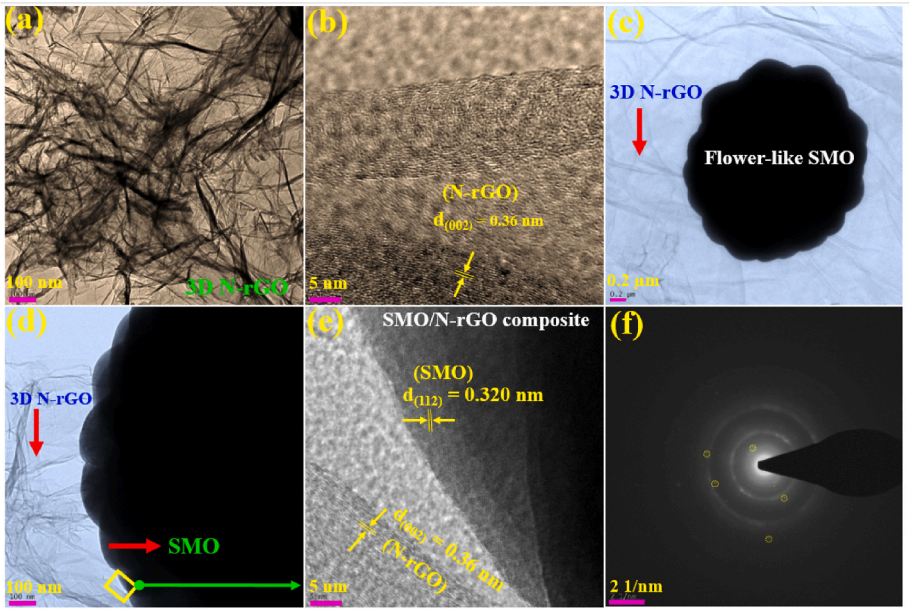

Fig. 2. (a) FE-TEM images and the corresponding (b) lattice fringe of 3D N-rGO. (c) Low and (d) high magnification images, (e) lattice fringe, and (f) SAED pattern of SMO/N-rGO composite.

(112) planes of the N-rGO and SMO MFs, respectively. Finally, the result in Fig. 2(f) shows the presence of circular patterns with some dots indicating the formation of a mixed amorphous phase of the N-rGO aerogel and the crystalline phase of the SMO MFs. Thus, the FE-SEM and FE-TEM results confirm the successful formation of SMO on N-rich rGO aerogel (SMO/N-rGO) by a simple synthesis method.

3.2. Structural characterization of SMO MFs, rGO, 3D N-rGO aerogel, and SMO/N-rGO composite

To determine the crystalline structural properties, a powder X-ray pattern was performed for the prepared samples, SMO MFs, rGO, N-rGO aerogel, and SMO/N-rGO composite, Fig. 3(A)(a-d). In Fig. 3(A)(a), the diffraction peaks of SMO MFs show the presence of multiple discrete peaks at angles of 18.0°, 27.6°, 29.7°, 33.2°, 38.1°, 45.1°, 47.6°, 51.5°, 55.9°, 57.1°, 61.7°, 69.7°, 71.8°, and 72.7°, which correspond to the hkl planes of (101), (112), (004), (200), (114), (204), (220), (116), (312), (224), (008), (400), (208), and (316), respectively. These data are in excellent agreement with the previously reported SMO planes and are also consistent with the JCPDS File No. 08–0482, suggesting that the prepared SMO MFs are in a tetragonal crystalline phase with space values a = b = 5.394 Å and c = 12.02 Å (space group *141/a*) [31]. Moreover, no additional impurities such as SrO or MoO_3 were observed, indicating that the SMO MFs are in the form of a pure and crystalline phase. The XRD patterns of rGO and N-rGO are shown in Fig. 3(B) (c, d), which demonstrate the presence of prominent diffraction peaks at 24.4° and 43.2° associated with the (002) and (100) planes corresponding to graphitic carbon [42]. This result shows that the pristine GO was successfully reduced into disordered and loosely stacked graphene sheets. The N-rich rGO (N-rGO) also shows analogous diffraction peaks with a slight variation in the 2θ values followed by a decrease in diffraction intensity, indicating that the presence of N leads to broad diffraction peaks in rGO (Fig. 3(B)(d)). Moreover, the interplanar spacing is larger than that of rGO, indicating that the N atoms are successfully introduced into rGO by π-π forces and covalent bonds, preventing the stacking of rGO layers and serving as supports for the rGO layers [48]. Finally, the XRD pattern in Fig. 3(A)(b), is consistent with the successful formation of the SMO/N-rGO composite. The intensity of the peaks of the SMO/N-rGO composite is lower than the SMO, while the peaks associated with N-rGO are significantly lower in the composite. This decrease in the peak intensity of N-rGO is mainly due to a decrease in the restacking of rGO, which may also be related to the presence of the anchored SMO MFs.

Fig. 3(C)(a) shows the Raman spectra of the as-prepared SMO MFs, rGO, N-rGO, and the SMO/N-rGO composite. Two groups of vibrational modes can be seen in the range 100–1800 cm^{-1}. Clearly, the $[MoO_4]^{2-}$ ions, which are present in the tetragonal scheelite structure, reduce the point group symmetry. As a result of this reduction, the degenerate vibrations are split into two groups, which affects the crystal field. Based on group theory analysis, the active degenerate vibrations of SMO are divided into 26 vibrations (Raman) = $3A_g + 5A_u + 5B_g + 3B_u + 5E_g + E_u$) [31]. These resulting vibrations are associated with the internal and external groups. This can be deduced from the stationary center of mass of $[MoO_4]^{2-}$, and another is related to the motion of Sr^{2+} in the rigid $[MoO_4]^{2-}$. As the $[MoO_4]^{2-}$ is tetrahedrally symmetric, the vibrational modes consist of translational and rotational modes. Of these, the 13 vibrational modes are Raman active. The external rotational modes are 185.7, 145.0, and 115.6 cm^{-1}, respectively. These vibrational modes depend on the lattice parameters and the covalent bonding between the Sr^{2+} and $[MoO_4]^{2-}$ ion groups. The internal translation modes at 898.6 $v_1(A_g)$, 849.5 $v_3(B_g)$, 800.9 $v_3(E_g)$, 386.2 $v_4(E_g)$, 372.5 $v_4(B_g)$, and 332.8 $v_2(B_g)$ cm^{-1} were found to belong to the different metal or metal-oxygen bonds. In particular, the peaks at 800.9 and 386.2 cm^{-1} indicate the doubly bonded oxygen (O–Mo–O) in the $[MoO_4]^{2-}$ ion group, while the others represent the Mo–O bond [31]. The well-resolved peaks of the SMO MFs indicate high crystallinity and are consistent with the predictions of the XRD analysis. The presence of alkaline earth metal cations (Sr^{2+}) can affect the Raman mode by influencing the crystal size and covalent bonding [49]. It has been found that the symmetric valence vibration of the $[MoO_4]^{2-}$ ionic groups expands in the Ba→Sr→Ca tetragonal scheelite sequence [49]. Therefore, it is clear that the combination of Sr^{2+} with $[MoO_4]^{2-}$ leads to a large interionic distance, which can cause better crystalline behavior for SMO. The Raman spectra

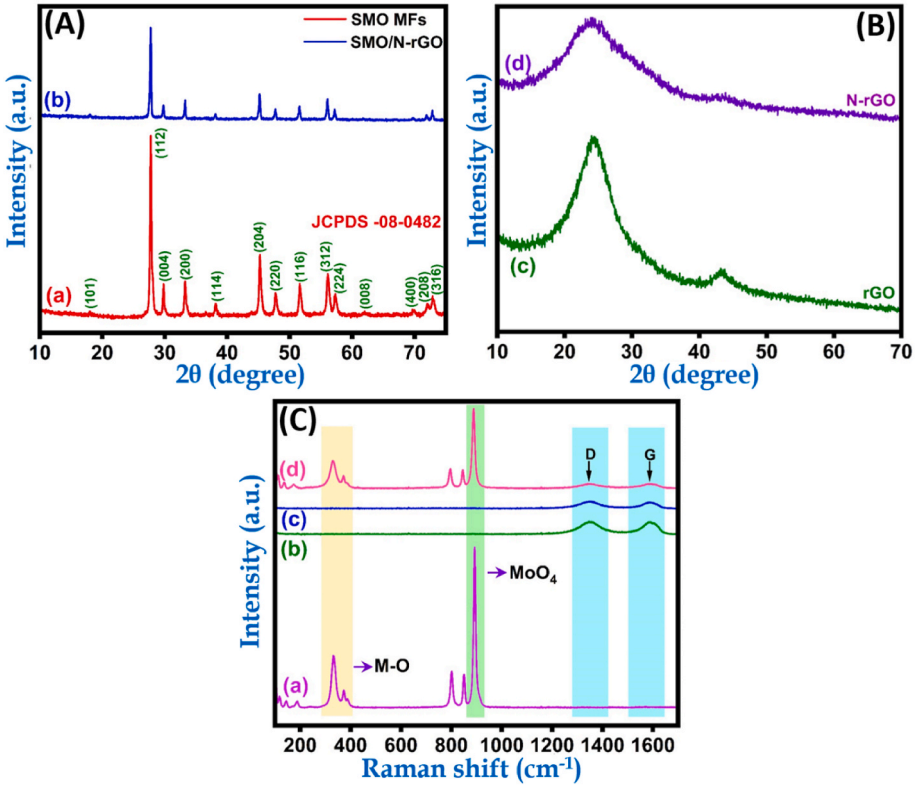

Fig. 3. (A, B) XRD patterns of (a) SMO MFs, (b) SMO/N-rGO composite, (c) rGO, and (d) N-rGO aerogel. (C) Raman spectra of (a) SMO MFs, (b) rGO, (c) N-rGO, and (d) SMO/N-rGO composite.

of both rGO and N-rGO are shown in Fig. 3(C) (b, c). It is known that carbon materials usually have two main Raman peaks: G and D bands. The G band arises from the scattering of the E_{2g} phonon vibrational symmetry of the sp^2 carbon atoms in the first-order graphite lattice. The D band is caused by A_{1g} and originates from the zone-bound phonons (conversion of sp^2 hybridized carbon to sp^3 hybridized carbon) [50]. Fig. 3(C) (b, c) shows the presence of a G band at 1589.2 cm^{-1} for both rGO and N-rGO due to the original graphite structure (defective sites). The D band appears at 1348.8 cm^{-1} for rGO, but at a slightly higher wavenumber of 1350.4 cm^{-1} for N-rGO. This is probably due to the stretching of the sp^2 bond pairs. The graphite structure consists of a highly ordered and defect-free structure, so the intensity of the G band is larger than that of the D band. The Raman spectra of the SMO/N-rGO composite can be seen in Fig. 3(C)(d), indicating a decrease in the intensity of both the SMO and N-rGO Raman signals. The I_D/I_G of SMO/N-rGO (1.1) is almost equal to that of N-rGO (1.13). From this analysis, it can be concluded that incorporating N-heteroatoms into the composite system simultaneously contributes to introducing defects, mainly due to the strong synergism between the SMO MFs and N-rGO aerogel. It is known that the heteroatoms can change the local charge density of carbon atoms, which can improve the electrochemical performance [42].

Following the XRD and Raman analysis, the valence state of the elements of the SMO/N-rGO composite was investigated using XPS analysis. Fig. 4(a) shows the overall survey spectrum of the composite in which only the elements Sr, Mo, C, N, and O are present. No additional peaks, indicative of impurities, were observed. The binding energy of Sr in the XPS spectrum (Fig. 4(b)) indicates two prominent peaks at 134.8 and 133.09 eV, which represent the two oxidation states of Sr in $3d_{3/2}$ and $3d_{5/2}$ doublets, respectively. The well-resolved peaks at 134.8 and 133.09 eV are typical of the binding energies of SMO MFs in their stable state. The deconvoluted spectrum of Mo 3d in Fig. 4(c) shows two high-intensity doublet peaks at 235.4 and 232.4 eV, which are assigned to the Mo^{6+} valence state and indicate the binding of Mo^{6+} with Sr^{2+} ions, leading to the successful formation of the SMO MFs. The magnified spectra of O 1s (Figure 4(d)) show three peaks at the binding energies of 533.2, 531.6, and 530.2 eV and these can be assigned to adsorbed oxygen species, deficits, and lattice oxygen in the O^{2-} state, respectively. Fig. 4(e) shows the splitting of four peaks from the C 1s spectra assigned to the C═C (284.7 eV), C–C/C–N (285.8 eV), C–O–C/C–OH (286.7 eV), C═O/C═N (288.0 eV) and COOH (289.0 eV) bonds, respectively. Fig. 4 (f) shows the high-resolution spectrum of N 1s, which can be deconvoluted into three distinct peaks with binding energy values of 395.7, 398.2, and 400.5 eV and these can be attributed to the presence of pyridinic N, pyrrolic N, and graphitic N in the N-rGO aerogel. Again, the XPS results confirm the formation of the SMO/N-rGO composite. Moreover, the introduction of N significantly improves the electron transport and Faradic process during an electrochemical sensing process [47]. The N_2 adsorption-desorption isotherms were performed to determine the BET surface area of the prepared SMO/N-rGO composite which is shown in Fig. S3. The isotherm curve for SMO/N-rGO represents the IUPAC IV isotherm with a distinct H3-type hysteresis loop, indicating the presence of abundant mesoporous and an external surface. The BET surface area for SMO/N-rGO was calculated to be 92.986 m^2/g, along with a pore volume distribution of 0.27 cm^3/g (Fig. S3 (a, b)). The resulting high surface area and mesopore nature of SMO/N-rGO is mainly due to the interconnected porous 3D aerogel network (close agreement with the analysis of FE-TEM).

3.3. Electrochemical properties of the different modified electrodes

EIS is a significant tool for studying the electron transfer properties of materials. Typical Nyquist plots are shown in Fig. 5(a) for bare GCE, N-rGO/GCE, SMO/GCE, and SMO/N-rGO/GCE. From the EIS results, the electrode modified with SMO/N-rGO has a low R_{ct} value of 89.7 Ω compared to GCE (331.6 Ω), N-rGO/GCE (224.4 Ω), and SMO/GCE (610.8 Ω), indicating very good electrochemical properties. This can be attributed to the strong synergistic effect between the N-rGO sheets and SMO MFs, resulting in more active sites, high conductivity, and larger contact area between electrode and electrolyte for NB detection. Further explanation of the EIS results can be seen in the supplemental file (Section *S3.1*).

The electrochemical performance was studied further by comparing the cyclic voltammograms (CV) recorded for the SMO/GCE, N-rGO/GCE, and SMO/N-rGO/GCE in the presence of 0.005 M $[Fe(CN)_6]^{3-/4-}$ with 0.1 M KCl at a scan rate of 50 mV s^{-1}. The CV results are shown in

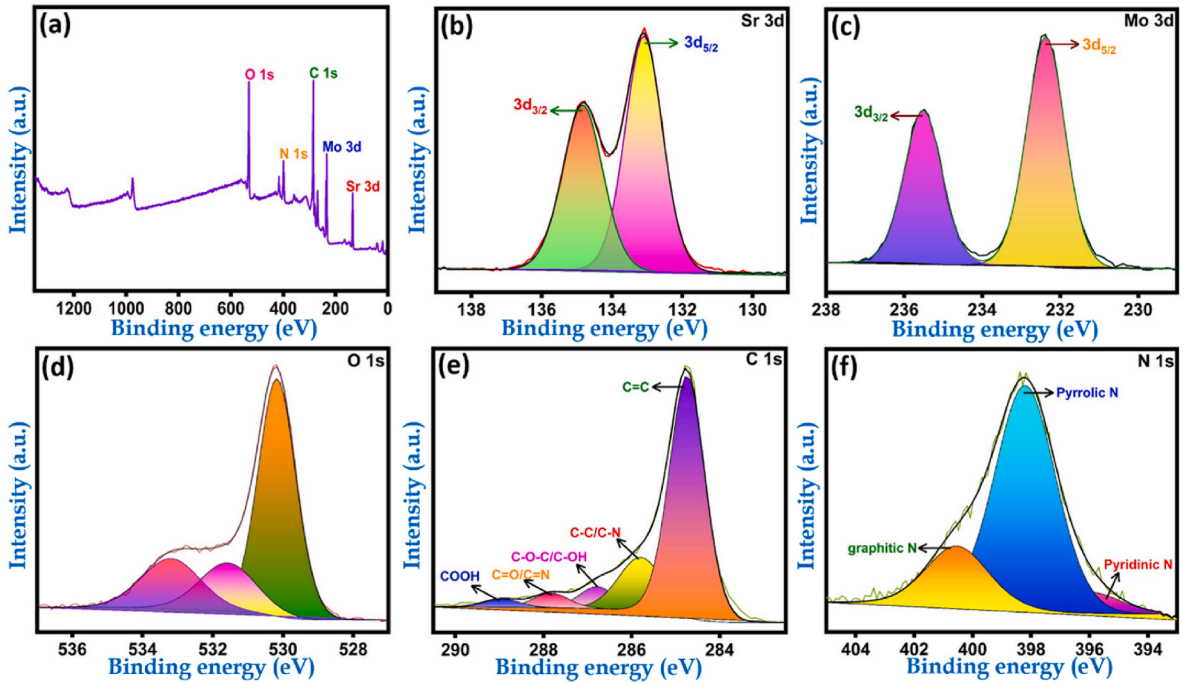

Fig. 4. XPS spectra of (a) survey scan (b) Sr 3d, (c) Mo 3d, (d) O 1s, (e) C 1s, and (f) N 1s.

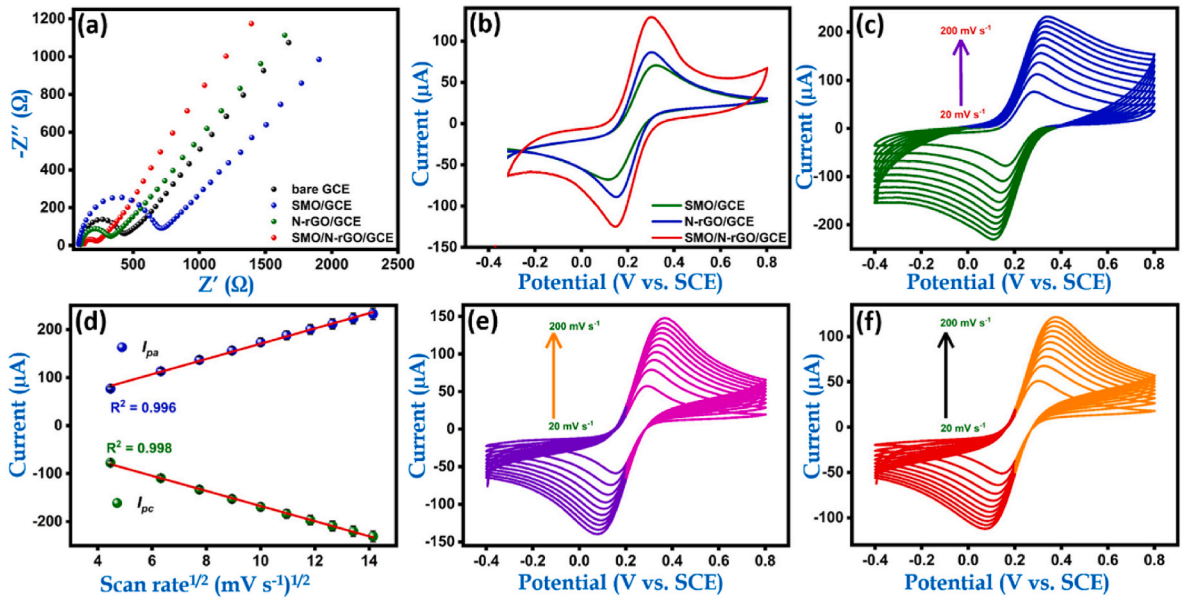

Fig. 5. (a) EIS and (b) CV for 0.005 M $[Fe(CN)_6]^{3-/4-}$ solution with 0.1 M KCl on bare GCE, SMO/GCE, N-rGO/GCE, and SMO/N-rGO/GCE. Scan rate: 50 mV s^{-1}. CVs of different scan rates from 20 to 200 mV s^{-1} on (c) SMO/N-rGO/GCE, (e) N-rGO/GCE, (f) SMO/GCE recorded in 0.005 M $[Fe(CN)_6]^{3-/4-}$ containing 0.1 M KCl. (d) The linear plot for I_{pa}, I_{pc} against the square root of the scan rate (SMO/N-rGO/GCE).

Fig. 5(b). The SMO/GCE shows weak redox pairs with an oxidation current (I_{pa}) and a reduction current (I_{pc}) of 70.7 and 68.1 μA, respectively, and a peak-to-peak separation ($\Delta E_p = E_{pa} - E_{pc}$) of 202 mV (green curve). Compared to the SMO-modified GCE, the current intensity is higher with the N-rGO/GCE (blue curve) with a slightly increased peak current of 87.9 (I_{pa}) and 90.1 μA (I_{pc}). The observed peak-to-peak separation is lower at 155 mV, indicating better electrical conductivity and a larger surface area. The highest redox peak currents ($I_{pa} = 130.8$ and $I_{pc} = 126.03$ μA) were observed with the SMO/N-rGO/GCE (red curve), which is ~ 1.4 times higher than N-rGO/GCE and ~ 2 times higher than SMO/GCE. These results show that the SMO/N-rGO/GCE significantly improves the electrochemical performance due to the large surface area and the strong synergistic effect between the SMO MFs and N-rGO sheets. Fig. 5(c, e, f) shows the CV curves at various sweep rates (20–200 mV s^{-1}) of SMO/GCE (linear plot, Fig. S4(a)), N-rGO/GCE (linear plot, Fig. S4(b)) and SMO/N-rGO/GCE (Fig. 5(d)) using 0.005 M $[Fe(CN)_6]^{3-/4-}$ solution as a redox probe with 0.1 M KCl. Fig. 5(e) shows the linear plot for the square root of scan rate versus I_{pa} and I_{pc} peak current of SMO/N-rGO/GCE. According to the Randles-Sevcik equation (1), the active electrochemical areas of the different modified electrodes can be calculated [51]:

$$I_{pa} = 2.691 \times 10^5 \, n^{3/2} \, D^{1/2} v^{1/2} \, AC \quad (1)$$

where C denotes the concentration of $[Fe(CN)_6]^{3-/4-}$ (mol/cm^3), A represents the electrochemical active surface area (cm^2), v is the scan rate (V s^{-1}), D denotes the diffusion coefficient of $[Fe(CN)_6]^{3-/4-}$ (0.076×10^{-4} cm^2 s^{-1}), n corresponds to the number of electrons transferred during the redox reaction, and I_{pa} is the anodic peak current. From equation (1), the electrochemically active areas of SMO/GCE, N-rGO/GCE, and SMO/N-rGO/GCE were calculated as 0.06, 0.07, and 0.13 cm^2, respectively. The computed active surface area of SMO/N-rGO/GCE is significantly larger than that of SMO or N-rGO, indicating that the composite possesses an increased electroactive surface area, to give a more efficient electrochemical sensor.

3.4. Electrochemical sensing of NB on the different modified GCE

The electrochemistry of NB at the GCE, SMO/GCE, N-rGO/GCE, SMO/rGO/GCE, and SMO/N-rGO/GCE modified electrodes was investigated using the CV technique. The experiments were performed in 0.05 M PBS (pH 7.0) in the presence of 300 μM NB at a sweep rate of 50 mV s^{-1} in the potential range from 0.4 to −1.1 V, and the results are summarized in Fig. 6 and Figure *S5*(b). As illustrated in Fig. 6(a), where the modified electrodes were cycled in the absence of NB, there is no redox and reduction waves. The voltammograms recorded with the N-rGO and the SMO/N-rGO composite exhibit capacitive characteristics, and this is due to the porous nature and high surface areas of these modifiers. In the presence of NB, the SMO/N-rGO/GCE shows a sharp and well-defined reduction peak (R_1) and gives the highest peak current compared to the other modified and unmodified electrodes, Fig. 6(b). This is more clearly illustrated in Fig. 6(c) where the I_{pc} is presented as a function of the corresponding modified electrodes, indicating the superior performance of the SMO/N-rGO/GCE. As shown in Fig. 6 (b, d red curve), the reduction wave is observed at an E_{pc} of −0.64 V in the existence of 300 μM NB with an I_{pc} of −125.7 μA for the SMO/N-rGO/GCE. The obtained cathodic peak (R_1) is related to the direct reduction of the nitro group (-NO_2) in nitrobenzene to phenylhydroxylamine which involves the transfer of an unequal number of electrons and protons [52]. In addition, two other peaks are also noted at a potential of −0.07 and −0.12 V, designated as O_1 and R_2, respectively (Fig. 6(d)). These peaks are related to the reversible conversion of phenylhydroxylamine (PH) to nitrozobenzene (NZB) with two electrons and two protons. The above two-step conversion of NB to phenylhydroxylamine/nitrozobenzene agrees with the previously reported article [52]. The overall electrochemical reduction and redox mechanism of NB is summarized in Fig. 6 (g). The cathodic peak current associated with R_1 is higher than that of R_2, indicating that the reduction at SMO/N-rGO/GCE in a neutral or basic medium preferentially leads to the formation of PH.

In summary, the I_{pc} (R_1) for SMO/N-rGO/GCE is 5.6, 5.3, 0.7, and 1.6 times higher than that for bare GCE, SMO/GCE, SMO/rGO/GCE (Fig. S5 (b)), and N-rGO/GCE, respectively, while the cathodic peak potential is shifted in the positive direction compared to bare GCE (136 mV), SMO/GCE (106 mV), SMO/rGO (17 mV), and N-rGO/GCE (14 mV). In addition, we also varied the ratio of N-rGO, e.g., 5, 10, and 15 mg for the composite preparation, and the electrochemical results for the detection of NB (300 μM) are shown in Fig. S5(a). From the results, it can be seen that the 10 mg N-rGO/SMO composites have a higher reduction peak current compared to the other ratios. Therefore, we selected 10 mg N-

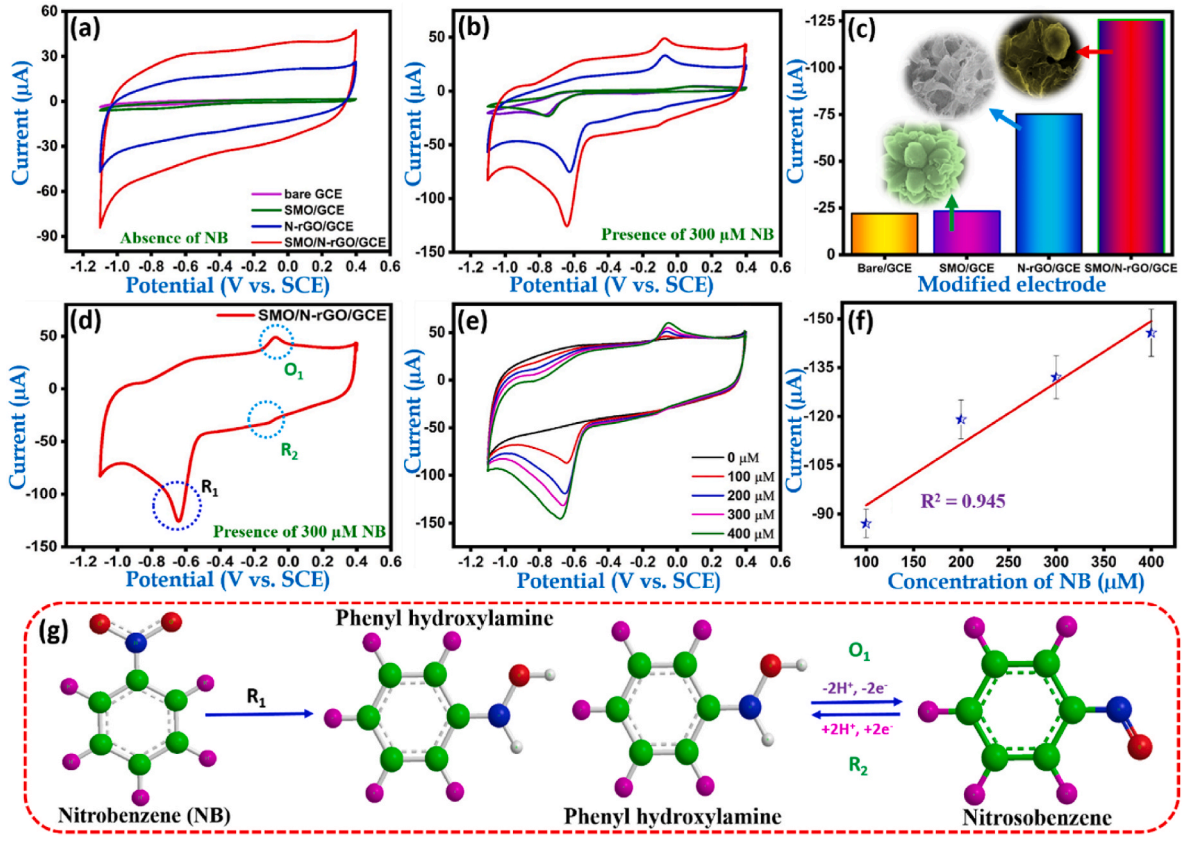

Fig. 6. CV curves of bare GCE, SMO/GCE, N-rGO/GCE, and SMO/N-rGO/GCE in (a) absence and (b, d) presence of 300 μM NB in 0.05 M PBS (pH 7.0) at a scan rate of 50 mV s^{-1}. (c) The bar graph for the different modified electrodes versus I_{pc}. (e) CV responses of SMO/N-rGO/GCE at different concentrations of NB from 100 to 400 μM, and (f) the calibration curve for the I_{pc} against different concentrations. (g) The overall electrochemical mechanism of NB at the SMO/N-rGO modified electrode.

rGO/SMO composites for further electrochemical measurements. These results clearly suggest that the larger surface area of the 3D N-rich porous rGO layers and the SMO MFs have a synergistic enhancement effect on the reduction of NB. The more thermodynamically favored E_{pc} and higher I_{pc} are evidence that the SMO/N-rGO modified electrode exhibits excellent electrochemical properties for the detection of NB. This is consistent with the superior conductivity of the 3D N-rich porous rGO, which can improve the electron transfer rate, and the larger surface area of the composite compared to the other modified electrodes, resulting in higher adsorption of NB molecules on the electrode surface, which in turn leads to higher reduction current values. These results are in good agreement with the EIS results. To verify the electrode stability, FE-SEM analysis was performed before and after the electrochemical reduction of NB in 0.05 M PBS (pH 7), which are shown in Fig. S6 (a) and (b). The morphology of the composite material (SMO/N-rGO) on the screen-printed carbon electrode (SPCE) was well preserved, and the electrode material did not deteriorate from the electrode surface even after the continued electrochemical reduction CV cycles of NB under the neutral medium, indicating the very stable nature of SMO/N-rGO composite.

To determine the effect of the concentration of NB on SMO/N-rGO/GCE, CV curves were measured while changing the concentration of NB from 0 to 400 μM at pH 7.0, with 0.05 M PBS at a sweep rate of 50 mV s^{-1} (Fig. 6(e)). The results show that the cathodic peak current increases with an increase in the concentrations of NB. The corresponding calibration plot of I_{pc} versus the concentration of NB is shown in Fig. 6(f) with a linear regression equation of $I_{pc} = -0.188 - 73.8$, and a correlation coefficient of $R^2 = 0.945$, indicating good linearity and suggesting that the proposed composites have an excellent ability to detect NB with a broader response range.

3.5. Influence of pH and scan rate

The pH of the supporting electrolyte is an important factor as it significantly affects the electrochemical behavior of NB at SMO/N-rGO/GCE. The CVs of NB were recorded at various pH values in 0.05 M PBS, ranging from a pH of 3.0–11.0 in the presence of 300 μM NB at a scan rate of 50 mV s^{-1} (Fig. 7(a and b)). The pH of the electrolyte had a significant effect on the electrochemical performance of NB on the SMO/N-rGO/GCE. It was found that the peak potential shifted more negatively when the pH increased from a lower to a higher value, confirming the participation of H^+ in the electrochemical reduction of NB. The corresponding bar graphs of pH and I_{pc}, and the linear plot of E_{pc} versus pH are shown in Fig. 7(b) and Fig. S7, respectively. The linear equation is $E_{pc} = -0.026$ pH - 0.49 ($R^2 = 0.916$). The observed slope value of −0.026 V per pH unit from the linear plot indicates that one proton and two electrons participated in the electrochemical reduction process of NB [53]. The bar graph in Fig. 7(b) shows that the I_{pc} of NB increases with pH from 3.0 to 7.0, and the peak current decreases at pH above 7.0. A higher reduction peak current was observed at pH 7.0, so 0.05 PBS (pH 7.0) was chosen as the optimal supporting electrolyte to achieve the best sensitivity in all subsequent electrochemical experiments for the detection of NB.

The influence of scan rate on the reduction peak current of NB was investigated using SMO/N-rGO/GCE. Fig. 7(c) shows the CV curves of SMO/N-rGO/GCE recorded at various sweep rates from 20 to 200 mV s^{-1} in 0.05 M PBS (pH 7.0) containing 300 μM NB. As shown in Fig. 7(d), the reduction peak (I_{pc}) gradually increases with an increase in scan rate in the range of 20–200 mV s^{-1}. The linear plot is plotted between the scan rate, the square root of the scan rate, and the reduction peak current (Fig. 7 (d) and (e)). The corresponding linear regression equations can

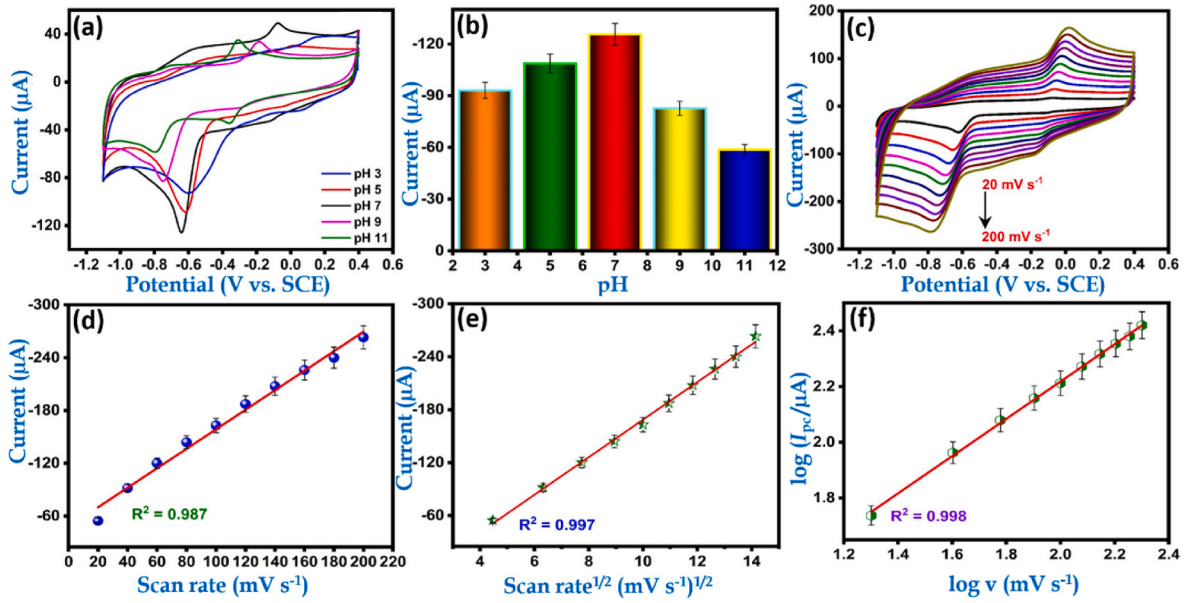

Fig. 7. (a) The CVs response of 300 μM NB at different pH values (0.05 M PBS, pH 3.0 to 11.0) on the SMO/N-rGO/GCE at a scan rate of 50 mV s^{-1}. (b) Bar graph for the different pH values and I_{pc}. (c) CVs of NB with SMO/N-rGO/GCE at different scan rates (20–200 mV s^{-1}) at pH 7.0. (d, e) Linear dependence plots of I_{pc} versus scan rate and the square root of the scan rates. (f) The linear relationship between the logarithm of scan rate and the logarithm of I_{pc}.

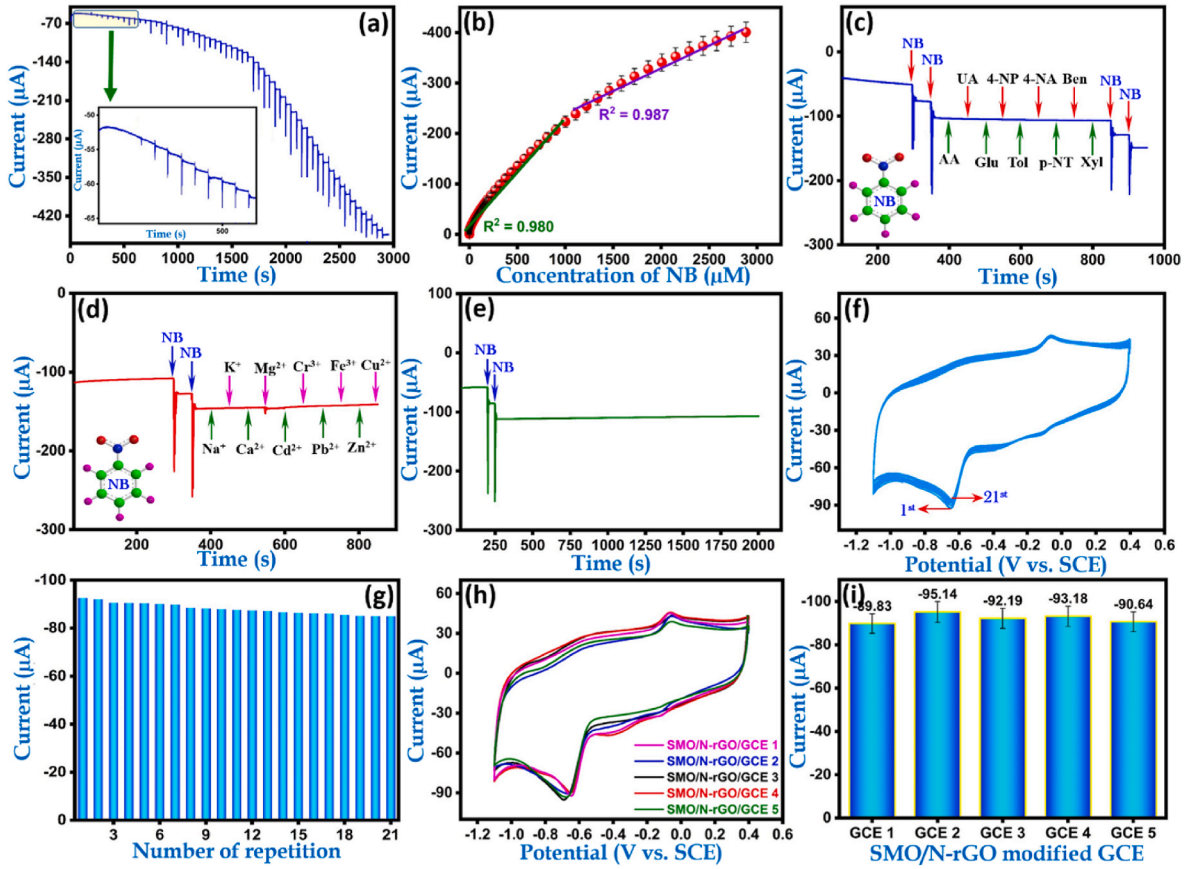

Fig. 8. (a) Amperometric (*i-t*) current response of SMO/N-rGO/RRDE after successive addition of NB (from 7.1 nM to 2884.9 μM) into constantly stirred 0.05 M PBS (pH 7.0) at an applied potential of −0.64 V. Inset is the magnified view of the amperometric response for the lower concentration of NB. (b) Calibration plot of I_{pc} and various concentrations of NB. (c, d) Effect of potentially interfering compounds (i.e., biomolecules, organic compounds, and ions) on the response of the NB sensor. (e) Operational stability of SMO/N-rGO/RRDE in the presence of 70 μM NB during the 2000 s test time in 0.05 M PBS (pH 7.0) at an applied potential of −0.64 V. (f) CV curves for the SMO/N-rGO/GCE repeatability studies for 21 independent measurements in pH 7.0 with 200 μM NB and (g) The corresponding intra-assay comparison in the form of a bar graph. (h) CVs response of five SMO/N-rGO/GCE sensors to 200 μM NB at pH 7.0 and (i) The corresponding bar graph of I_{pc} and five different electrodes.

be expressed as I_{pc} (μA) = −1.10 - 47.80 (R^2 = 0.987) (Fig. 7(d)) and I_{pc} (μA) = −21.30 $v^{1/2}$ (mV s^{-1})$^{1/2}$ + 44.23 (R^2 = 0.997) (Fig. 7(e)). From the linear plots, the best fit was obtained for the square root of the scan rate versus the reduction peak current, indicating that the reduction current of NB is a diffusion-controlled process at the surface of SMO/N-rGO/GCE. Moreover, a good linear relationship was observed between the logarithm of the reduction peak current (log I_{pc}) and the log scan rate (log v) with a linear equation of log I_p = 0.66 log v + 0.87 (R^2 = 0.998). The observed slope value of 0.66 (Fig. 7(f)) from the linear plot is reasonably close to the theoretical value of 0.5, indicating a diffusion-controlled process. These results indicate that the reduction of NB at the SMO/N-rGO/GCE is primarily controlled by diffusion and supported by adsorption. In addition, the peak potential depends on the scan rate. Fig. 7(c) shows that the reduction peaks potential shifts to more negative values as the scan rate increases, indicating that the reduction process is irreversible (R_1) [54].

3.6. Amperometric (i-t) determination of NB on SMO/N-rGO modified electrode

Amperometric measurements (*i-t*) are one of the most sensitive, selective, and reliable electrochemical techniques for the determination of target molecules. Fig. 8(a) shows a typical amperometric response of the SMO/N-rGO composite modified rotating ring disc electrode (RRDE) to the successive addition of NB (from 7.1 nM to 2884.9 μM) into a constantly stirred (rotation speed 1600 rpm) 0.05 M PBS (pH 7.0) solution at an applied potential of −0.64 V. With each successive injection of NB into the electrolyte a well-defined signal is observed and a near steady state current is achieved within 5 s, as illustrated in the inset in Fig. 8(a). Fig. 8(a, inset) shows the magnified view of the reduction current response at a low concentration of NB. On plotting the steady state current as a function of the concentration of NB, a calibration curve was obtained, as shown in Fig. 8(b). The calibration plot shows two linear response ranges from 7.1 nM to 1001.9 μM (lower concentration) and from 1108.9 to 2578.2 μM (higher concentration). The corresponding linear regression equations are I_{pc} (μA) = −0.226 C (μM) - 15.56 (R^2 = 0.980) and I_{pc} (μA) = 0.097 C (μM) – 139.54 (R^2 = 0.987), respectively. These results demonstrate that the SMO/N-rGO/RRDE can detect NB at low and higher concentrations. The detection limit (LOD) was calculated by using the following equation: LOD = $3S_{bl}$/b, where 'S_{bl}' is the standard deviation of the blank signal and 'b' is the slope of the calibration curve. The LOD and sensitivity were calculated as 2.5 nM (signal-to-noise ratio, S/N = 3) and 1.15 μA μM^{-1} cm^{-2}, respectively. The sensitivity is calculated from the slope of the calibration plot divided by the working area of the electrode (GCE). To evaluate the novelty and superiority of the NB sensor based on SMO/N-rGO composite material, we prepared a comparison table for the analytical performance (*i.e.*, LOD, sensitivity, and linear response range) with the previously reported NB sensors, and this comparison is made in Table S2. The results from the table show that the SMO/N-rGO modified RRDE has very good analytical performance and compares favorably with the existing NB sensors, with an impressive LOD value. This comparison clearly shows that the SMO MFs on the 3D N-rich porous N-rGO composite provides a compatible microenvironment for the reduction of NB.

3.7. Evaluation of selectivity, reproducibility, repeatability, and stability

To evaluate the anti-interference ability of the SMO/N-rGO composite, potential interfering substances such as biomolecules, organic compounds (Fig. 8(c)), and cations (Fig. 8(d)) that are likely to act as interferences in real-time water analysis, were selected and investigated using the amperometric (*i-t*) method. The amperometric experiments were carried out under optimal conditions by adding the interfering compounds at concentrations that were 2-fold higher than NB (70 μM). The interferences included biomolecules (ascorbic acid (AA), uric acid (UA) and glucose (Glu)), organic compounds with similar functional groups (4-nitrophenol (4-NP), toluene (Tol), 4-nitroaniline (4-NA), p-nitro toluene (p-NT), benzaldehyde (Ben), xylene (Xyl)), and cations present in aquatic systems (Na^+, K^+, Ca^{2+}, Mg^{2+}, Cd^{2+}, Cr^{3+}, Pb^{2+}, Fe^{3+}, Zn^{2+}, and Cu^{2+}). As shown in Fig. 8(c and d), the steady-state current response of the interfering compounds is much lower than that generated by NB. Only a slight current response was observed when Mg^{2+} was added to the electrolyte, but this current response is within 3% of the initial current response of NB. These results show that the electrode modified with SMO/N-rGO has excellent selectivity for NB sensing even when the above biomolecules, cations, and other organic molecules with nitro-functional groups are present.

The stability of the electrode modified with the SMO/N-rGO composite in the presence of 70 μM NB was tested at an applied potential of −0.64 V for the 2000s. As shown in Fig. 8(e) the current remains constant indicating excellent stability over 2000 s. For the repeatability tests, the CVs of 200 μM NB were measured more than 20 times using a SMO/N-rGO/GCE under identical conditions. Fig. 8(f) shows the CV curves for the repeatability test, and Fig. 8(g) shows the corresponding bar graph. As shown in Fig. 8(f and g), the relative standard deviation (RSD) is only 2.65%, indicating good repeatability of the fabricated electrode. Five different SMO/N-rGO/GCE sensors were fabricated individually by the same method to investigate reproducibility. The reduction peak current of NB in 0.05 M PBS was measured in the existence of 200 μM NB (Fig. 8(h)), while the corresponding bar graph for the different electrodes is provided in Fig. 8(i). Acceptable reproducibility was achieved with the RSD computed as 2.03%. These results clearly demonstrate that the selectivity, stability, repeatability, and reproducibility of the SMO/N-rGO/GCE fabricated in this analysis are acceptable. These results guarantee the sustainability and usefulness of this electrode in real water sample analysis. Moreover, the reusability of the proposed sensor is an essential factor that determines the sensor's life in real-time applications. For this reason, the reusability experiment of the SMO/N-rGO/GCE sensor was carried out in the presence of 200 μM NB with 0.05 M PBS (pH 7) for four cycles. The results obtained are shown in the bar graph in Fig. S8. A slight change in the cathodic current response was observed, less than 3% of the original current response. This indicates that the sensor can be regenerated at least four times by simply rinsing with deionized water at room temperature.

3.8. Detection of NB in the real environmental samples

To assess the reliability and feasibility of the prepared SMO/N-rGO modified electrode, we conducted recovery studies on various water samples, including tap and lake water under the optimal conditions using the amperometry technique. The collected lake and tap water samples were directly used to analyze the real samples without pretreatment by the standard addition method. The results are presented in Table S3. No electrochemical response of NB was observed in the collected lake and tap water samples which indicates the absence of NB in the water samples. Therefore, a known concentration of NB was added to the water samples, and the amperometric signal was recorded. The results from Table S3 show that the recoveries due to the added NB in the water sample ranged from 96.1 to 99.6%. These recoveries are satisfactory and indicate that the SMO/N-rGO modified electrode sensor has excellent practicality and can be used to determine the NB content in real water samples with no prior work-up.

4. Conclusion

In summary, SMO MFs anchored on 3D N-rGO aerogel were synthesized using a simple and sustainable methodology. The resulting SMO/N-rGO composite was employed in the electrochemical sensing of NB giving high selectivity and the detection of trace amounts of NB in the vicinity of 2.5 nM. To the best of our knowledge, this marks the first report on the exploitation of the synergistic interactions between SMO MFs and 3D N-rGO to give a high-performing electrochemical sensor for

the detection of NB in real water samples. In particular, the SMO/N-rGO sensor exhibited good repeatability, reproducibility and is reusable with excellent stability. The promising electrochemical properties of the SMO/N-rGO composite was attributed to the large surface area of the N-rich rGO aerogel and the high electronic conductivity of the SMO MFs.

This sensor, which is inexpensive and easy to manufacture, has the potential to be used in the detection of trace amounts of NB in wastewater samples, rivers, lakes, and other aquatic systems adjacent to NB-contaminated sites. This is relevant to society and important for accurate decision-making associated with the remediation and protection of NB-contaminated sites.

Credit author statement

Raj Karthik: Conceptualization, Methodology, Experimental operation, Data curation, Analysis, Writing - original draft. **Prajakta R. Chavan:** Conceptualization, Methodology, Experimental operation, Data curation, Analysis, Writing - original draft. **Ramaraj Sukanya**: Conceptualization, Methodology, Investigation, Validation, Data curation, Analysis, Writing-original draft, **Ganesh Dhakal**: Graphical abstract drawing, **Jae-Jin Shim**: Project administration and Supervision. **Carmel B. Breslin**: Data curation, Analysis, Writing - original draft, Editing, and Supervision.

Declaration of competing interest

The authors declare that they have no known competing financial interests or personal relationships that could have appeared to influence the work reported in this paper.

Data availability

Data will be made available on request.

Acknowledgments

This study was supported by the National Research Foundation (NRF) of the Republic of Korea under the frameworks of the Priority Research Centers Program (NRF-2014R1A6A1031189) and the Regional University Superior Scientist Research Program (NRF-2020R1I1A3073981) funded by the Ministry of Education, the Republic of Korea.

Appendix A. Supplementary data

Supplementary data to this article can be found online at https://doi.org/10.1016/j.compositesb.2023.110649.

References

[1] Chen B, Wenhai H. Effect of background electrolytes on the adsorption of nitroaromatic compounds onto bentonite. J Environ Sci 2009;21:104–52.
[2] Haigler BE, Spain JC. Biotransformation of nitrobenzene by bacteria containing toluene degradative pathways. Appl Environ Microbiol 1991;57(11):3156–62.
[3] Cropek D, Kemme PA, Makarova OV, Chen LX, Raj T. Selective photocatalytic decomposition of nitrobenzene using surface modified TiO_2 nanoparticles. J Phys Chem C 2008;112:8311–8.
[4] Mahony AMO, Wang J. Nanomaterial-based electrochemical detection of explosives: a review of recent developments. Anal Methods 2013;5:429–4309.
[5] Zhao Y, Lin L, Hong M. Nitrobenzene contamination of groundwater in a petrochemical industry site. Front Environ Sci Eng 2019;13:29.
[6] Wcisło E, Bronder J. Health risk assessment for the residential area adjacent to a former chemical plant. Int J Environ Health Res 2022;19(5):2590.
[7] Li M, Peng X, Liu X, Wang H, Zhang S, Hu G. Single-atom niobium doped BCN nanotubes for highly sensitive electrochemical detection of nitrobenzene. RSC Adv 2021;11:28988.
[8] Velmurugan M, Karikalan N, Chen SM, Dai ZC. Studies on the influence of b-cyclodextrin on graphene oxide and its synergistic activity to the electrochemical detection of nitrobenzene. J Colloid Interface Sci 2017;490:365–71.
[9] Wang GY, Yang LL, Li Y, Song H, Ruan WJ. A luminescent 2D coordination polymer for selective sensing of nitrobenzene. Dalton Trans 2013;42:12865–8.
[10] Chen X, Cheng X, Gooding JJ. Detection of trace nitroaromatic isomers using indium tin oxide electrodes modified using cyclodextrin and silver nanoparticles. Anal Chem 2012;84:8557–856.
[11] Wang SP, Chen HJ. Separation, and determination of nitrobenzenes by micellar electrokinetic chromatography and high-performance liquid chromatography. J Chromatogr A 2002;979:439–46.
[12] Niazi A, Yazdanipour A. Spectrophotometric simultaneous determination of nitrophenol isomers by orthogonal signal correction and partial least squares. J Hazard Mater 2007;146:421–7.
[13] Beitollahi H, Tajik S, Nejad FG, Safaei M. Recent advances in ZnO nanostructure-based electrochemical sensors and biosensors. J Mater Chem B 2020;8(27):5826–44.
[14] Mazloum-Ardakani M, Taleat Z, Khoshroo A, Beitollahi H, Dehghani H. Electrocatalytic oxidation and voltammetric determination of levodopa in the presence of carbidopa at the surface of a nanostructure based electrochemical sensor. Biosens Bioelectron 2012;35(1):75–81.
[15] Raoof JB, Ojani R, Beitollahi H, Hosseinzadeh R. Electrocatalytic oxidation and highly selective voltammetric determination of L-cysteine at the surface of a 1-[4-(ferrocenyl ethynyl) phenyl]-1-ethanone modified carbon paste electrode. Anal Sci 2006;22(9):1213–20.
[16] Tajik S, Beitollahi H, Nejad FG, Sheikhshoaie I, Nugraha AS, Jang HW, Yamauchi Y, Shokouhimehr M. Performance of metal–organic frameworks in the electrochemical sensing of environmental pollutants. J Mater Chem 2021;9(13):8195–220.
[17] Mazloum-Ardakani M, Beitollahi H, Ganjipour B, Naeimi H. Novel carbon nanotube paste electrode for simultaneous determination of norepinephrine, uric acid and d-penicillamine. Int J Electrochem Sci 2010;5:531–46.
[18] Tajik S, Beitollahi H, Nejad FG, Kirlikovali KO, Van Le Q, Jang HW, Varma RS, Farha OK, Shokouhimehr M. Recent electrochemical applications of metal–organic framework-based materials. Cryst Growth Des 2020;20(10):7034–64.
[19] Beitollahi H, Mahmoudi Moghaddam H, Tajik S. Voltammetric determination of bisphenol A in water and juice using a lanthanum (III)-doped cobalt (II, III) nanocube modified carbon screen-printed electrode. Anal Lett 2019;52(9):1432–44.
[20] Foroughi MM, Beitollahi H, Tajik S, Akbari A, Hosseinzadeh R. Electrochemical determination of N-acetylcysteine and folic acid in pharmaceutical and biological samples using a modified carbon nanotube paste electrode. Int. J. Electrochem. 2014;9:8407.
[21] Tajik S, Orooji Y, Ghazanfari Z, Karimi F, Beitollahi H, Varma RS, Jang HW, Shokouhimehr M. Nanomaterials modified electrodes for electrochemical detection of Sudan I in food. J Food Meas Char 2021;15:3837–52.
[22] Tajik S, Beitollahi H, Nejad FG, Dourandish Z, Khalilzadeh MA, Jang HW, Venditti RA, Varma RS, Shokouhimehr M. Recent developments in polymer nanocomposite-based electrochemical sensors for detecting environmental pollutants. Ind Eng Chem Res 2021;60(3):1112–36.
[23] Karthik R, Balamurugan K, Chen SM, Sukanya R, Chavan Prajakta R, Shim JJ, et al. Investigation of the electrocatalytic activity of bismuth-substituted pyrochlore $Y_2Sn_2O_7$ for the voltammetry determination of the antipsychotic drug. Mater Today Chem 2022;26:101117.
[24] Karuppaiah B, Jeyaraman A, Chen SM, Chavan Prajakta R, Karthik R, Hasan M, et al. Effect of bismuth doping on zircon-type gadolinium vanadate: effective electrocatalyst for determination of hazardous herbicide mesotrione. Chemosphere 2023;313:137543.
[25] Karuppaiah B, Jeyaraman A, Chen SM, Chavan Prajakta R, Karthik R, Shim JJ, et al. Design and synthesis of nickel-doped cobalt molybdate microrods: an effective electrocatalyst for the determination of antibiotic drug ronidazole. Environ Res 2023:115343.
[26] Li M, Peng X, Liu X, Wang H, Zhang S, Hu G. Single-atom niobium doped BCN nanotubes for highly sensitive electrochemical detection of nitrobenzene. RSC Adv 2021;11(46):28988–95.
[27] Sang Y, Cui Y, Li Z, Ye W, Li H, Zhao XS, Guo P. Electrochemical reaction of nitrobenzene and its derivatives on glassy carbon electrode modified with $MnFe_2O_4$ colloid nanocrystal assemblies. Sens Actuators B Chem 2016;234:46–52.
[28] Zhao X, Li A, Quan X, Chen S, Yu H, Zhang S. Efficient electrochemical reduction of nitrobenzene by nitrogen doped porous carbon. Chemosphere 2020;238:124636.
[29] Dai J, Yao L, Gao X, Bai S, Chen X, Li L, Song J, Yang H. To achieve ultrasensitive electrochemical detection of mercury ions employing metallic 1T-MoS_2 nanosheets. Electrochim Acta 2020;355:136800.
[30] Hira SA, Nallal M, Park KH. Fabrication of PdAg nanoparticle infused metal-organic framework for electrochemical and solution-chemical reduction and detection of toxic 4-nitrophenol. Sens Actuators B Chem 2019;298:126861.
[31] Karthik R, Karikalan N, Chen SM, Kumar JV, Karuppiah C, Muthuraj V. Assessment of divergent functional properties of seed-like strontium molybdate for the photocatalysis and electrocatalysis of the postharvest scald inhibitor diphenylamine. J Catal 2017;352:606–16.
[32] Chen TW, Kumar JV, Chen SM, Mutharani B, Karthik R, Nagarajan ER, Muthuraj V. Rational construction of novel rose petals-like yttrium molybdate nanosheets: a Janus catalyst for the detection and degradation of cardioselective β-blocker agent acebutolol. Chem Eng J 2019;359:1472–85.
[33] Kumar JV, Karthik R, Chen SM, Kokulnathan T, Sakthinathan S, Muthuraj V, Chiu TW, Chen TW. Highly selective electrochemical detection of antipsychotic drug chlorpromazine in drug and human urine samples based on peas-like strontium molybdate as an electrocatalyst. Inorg Chem Front 2018;5(3):643–55.
[34] Karthik R, Kumar JV, Chen SM, Kokulnathan T, Yang HY, Muthuraj V. Design of novel ytterbium molybdate nanoflakes anchored carbon nanofibers: challenging

sustainable catalyst for the detection and degradation of assassination weapon (Paraoxon-Ethyl). ACS Sustainable Chem Eng 2018;6(7):8615–30.
[35] Tarcan R, Todor-Boer O, Petrovai I, Leordean C, Astilean S, Botiz I. Reduced graphene oxide today. J Mater Chem C 2020;8(4):1198–224.
[36] Kim MY, Lee JW, Lee JY, Myung NV, Kwon SH, Lee KH. Highly stable potentiometric sensor with reduced graphene oxide aerogel as a solid contact for detection of nitrate and calcium ions. J Electroanal Chem 2021;897:115553.
[37] Wang Q, Wang J, Zhao Y, Zhao Y, Yan J, Deng Z, Zhang H, Zhao W, Tian J, Yun J, Zhang Z. NiO/$NiFe_2O_4$@ N-doped reduced graphene oxide aerogel towards the wideband electromagnetic wave absorption: experimental and theoretical study. Chem Eng J 2022;430:132814.
[38] Kim MY, Park H, Lee JY, Lee JY, Myung NV, Lee KH. Hierarchically palladium nanoparticles embedded polyethyleneimine–reduced graphene oxide aerogel (RGA–PEI–Pd) porous electrodes for electrochemical detection of bisphenol A and H_2O_2. Chem Eng J 2022;431:134250.
[39] Ma X, Gao F, Liu G, Xie Y, Tu X, Dai YR, Qu F, Wang W, Lu L. Sensitive determination of nitrite by using an electrode modified with hierarchical three-dimensional tungsten disulfide and reduced graphene oxide aerogel. Microchim Acta 2019;86:291.
[40] Ma X, Gao F, Liu G, Xie Y, Tu X, Li Y, Dai R, Qu F, Wang W, Lu L. Sensitive determination of nitrite by using an electrode modified with hierarchical three-dimensional tungsten disulfide and reduced graphene oxide aerogel. Microchim Acta 2019;186:1–9.
[41] Liu Q, Zhang L, Chen H, Jin J, Wang N, Wang Y, Sui D. Sulfur and nitrogen co-doped three-dimensional graphene aerogels for high-performance supercapacitors: a head to head vertical bicyclic molecule both as pillaring agent and dopant. Appl Surf Sci 2021;565:150453.
[42] Liu X, Lu Z, Huang X, Bai J, Li C, Tu C, Chen X. Self-assembled S, N co-doped reduced graphene oxide/MXene aerogel for both symmetric liquid-and all-solid-state supercapacitors. J Power Sources 2021;516:230682.
[43] Moradpour H, Beitollahi H, Nejad FG, Di Bartolomeo A. Glassy carbon electrode modified with n-doped reduced graphene oxide sheets as an effective electrochemical sensor for amaranth detection. Mater 2022;15(9):3011.
[44] Feng S, Yu L, Yan M, Ye J, Huang J, Yang X. Holey nitrogen-doped graphene aerogel for simultaneously electrochemical determination of ascorbic acid, dopamine and uric acid. Talanta 2021;224:121851.
[45] Denis PA, Huelmo CP. Structural characterization and chemical reactivity of dual doped graphene. Carbon 2015;87:106–15.
[46] Bag S, Mondal B, Das AK, Raj CR. Nitrogen and sulfur dual-doped reduced graphene oxide: synergistic effect of dopants towards oxygen reduction reaction. Electrochim Acta 2015;163:16–23.
[47] Dai S, Liu Z, Zhao B, Zeng J, Hu H, Zhang Q, Chen D, Qu C, Dang D, Liu M. A high-performance supercapacitor electrode based on N-doped porous graphene. J Power Sources 2018;387:43–8.
[48] Hou S, Cai X, Wu H, Yu X, Peng M, Yan K, Zou D. Nitrogen-doped graphene for dye-sensitized solar cells and the role of nitrogen states in triiodide reduction. Energy Environ Sci 2013;6(11):3356–62.
[49] Oh WC, Park CY, Jeon JW, Lim CS. Solid-state metathetic synthesis of strontium molybdate particles assisted by microwave irradiation. Asian J Chem 2012;24(7).
[50] Cao X, Yan S, Hu F, Wang J, Wan Y, Sun B, Xiao Z. Reduced graphene oxide/gold nanoparticle aerogel for catalytic reduction of 4-nitrophenol. RSC Adv 2016;6(68):64028–38.
[51] Sukanya R, Sakthivel M, Chen SM, Chen TW. A new type of terbium diselenide nano octagon integrated oxidized carbon nanofiber: an efficient electrode material for electrochemical detection of morin in the food sample. Sensor Actuator B Chem 2018;269:354–67.
[52] Li SS, Fang JH, Li L, Zhu M, Zhang F, Zhang BY, Jiang TJ, Zhang YX. An ultra-sensitive electrochemical sensor of Ni/Fe-LDH toward nitrobenzene with the assistance of surface functionalization engineering. Talanta 2021;225:122087.
[53] van Leeuwen SM, Blankert B, Kauffmann JM, Karst U. Prediction of clozapine metabolism by on-line electrochemistry/liquid chromatography/mass spectrometry. Anal Bioanal Chem 2005;382:742–50.
[54] Janjua NK, Akhter Z, Jabeen F, Iftikhar B. Cyclic voltammetric investigation of interactions between bisnitroaromatic compounds and ds. DNA J Korean Chem Soc 2014;58(2):153–9.